Reversal of Band-ordering Leads to High Hole Mobility in Strained *p*-type ScN

Sourav Rudra[1,2], Dheemahi Rao[1,2], Samuel Poncé[3] and Bivas Saha[1,2,4]

[1]*Chemistry and Physics of Materials Unit, Jawaharlal Nehru Centre for Advanced Scientific Research, Bangalore 560064, India.*
[2]*International Centre for Materials Science, Jawaharlal Nehru Centre for Advanced Scientific Research, Bangalore 560064, India.*
[3]*European Theoretical Spectroscopy Facility, Institute of Condensed Matter and Nanosciences, Université catholique de Louvain, Chemin des Étoiles 8, B-1348, Louvain-la-Neuve, Belgium*
[4]*School of Advanced Materials (SAMat), Jawaharlal Nehru Centre for Advanced Scientific Research, Bangalore 560064, India.*

Low hole mobility of nitride semiconductors is a significant impediment in realizing their high-efficiency device applications. Scandium nitride (ScN), an emerging rocksalt indirect bandgap semiconductor, suffers from low hole mobility. Utilizing the *ab initio* Boltzmann transport formalism including spin-orbit coupling, here we show the dominating role of ionized impurity scattering in reducing the hole mobility in ScN thin films. We suggest a route to increasing the hole mobility by reversing the band ordering through strain engineering. Our calculation shows that the bi-axial tensile strain in ScN lifts the split-off hole band above the heavy hole and light hole bands, leading to a lower hole-effective mass and increasing mobility. Along with the impurity scattering, Fröhlich interaction also plays a vital role in the carrier scattering mechanism due to the polar nature of ScN. Increased hole mobility in ScN will lead to higher efficiencies in thermoelectric, plasmonics, and neuromorphic computing devices.

Keywords: Electron-phonon coupling, first-principles calculations, carrier transport, Boltzmann transport, Ionized-impurity scattering, Strained-induced band ordering reversal, Scandium Nitride (ScN)

Correspondence is to be addressed to bsaha@jncasr.ac.in and bivas.mat@gmail.com

The mobility of charge carriers (electrons and holes) in semiconductors is a fundamental property that determines device efficiencies. Semiconductors with high electron mobilities are used in transistors, light-emitting diodes, lasers, high-mobility electron transistors, and many other electronic and optoelectronic devices [1–5]. However, III-V semiconductors, particularly nitrides, exhibit low hole mobilities due to their large valence band (VB) effective mass and heavy carrier scattering [6,7]. For example, extensive research over the last three decades has resulted in a high electron mobility of 1265-2000 cm^2/Vs at room temperature in GaN [8,9]. However, hole mobility has remained low to ~ 40 cm^2/Vs at room temperature [10,11]. Moreover, since most nitride semiconductors require hole dopants to compensate for their high electron concentration and to achieve *p*-type carrier conduction [12,13], ionized-impurity scattering also plays an important role [14,15]. Therefore, understanding the various carrier scattering mechanisms and developing new strategies to increase hole mobility in semiconductors remains an open challenge.

Scandium nitride (ScN) is an emerging group-III(B) rocksalt indirect bandgap semiconductor [16] and has attracted much attention for its high thermoelectric power factor [17], as a seed layer for defect-free GaN growth [18], and epitaxial metal/semiconductor superlattice development [19]. Like most other transition metal nitrides, ScN is mechanically hard (~ 24 GPa.), corrosion resistant, and exhibits an indirect $\Gamma - X$ bandgap of 0.9 eV and direct $\Gamma - \Gamma$ bandgap of 2.1-2.6 eV [20–22]. Recent research has demonstrated that ScN exhibits low-loss and high-quality plasmon- and phonon-polaritons in the short-wavelength infrared and long-wavelength infrared spectral ranges, respectively with high *figure-of-merits* [23]. Persistent photoconductivity in ScN has also been used to demonstrate optoelectronic artificial synaptic devices with memory and learning abilities [24]. Theoretical calculations have also predicted that ScN would be an excellent barrier layer in magnetic tunnel junctions [25]. Schottky diodes of ScN with elemental metals such as Au and Ag have been experimentally demonstrated recently [26].

Traditionally, molecular beam epitaxy or magnetron sputter-deposited ScN thin films exhibit a high *n*-type carrier concentration in the (2-5) × 10^{20} cm^{-3} range and electron mobility of 90-130 cm^2/Vs at room temperature [27]. However, utilizing the hybrid vapor phase epitaxy (HVPE), the highest electron mobility of 284 cm^2/Vs has been achieved in micron-sized thick ScN films at room temperature [28]. Mg-hole doping has been used successfully to compensate for the high electron concentration and to achieve *p*-type ScN thin films. The highest hole concentration of 2.2 × 10^{20} cm^{-3} and hole mobility of 21 cm^2/Vs has been reported in *p*-type ScN, suggesting ionization of most hole-dopants [29].

The low hole mobility (about four-to-five times smaller compared to similar *n*-type films) of ScN is a significant limitation in realizing its device application. However, until now, little attention has been paid to understanding the microscopic origin of low hole mobility and design strategies to improve them. In this work, we calculate the valence band from first-principles with different scattering mechanisms that are responsible for the low hole mobility in *p*-type ScN. We suggest a practical strategy to overcome this hindrance using the *ab initio* Boltzmann transport formalism.

First-principle electronic structure calculation using the spin-orbit coupling (SOC) and density-functional perturbation theory (DFPT) for phonons are carried out using the QUANTUM ESPRESSO [30] package within the PBE parametrization [31] of the generalized gradient approximation (GGA) for the exchange-correlation with optimized norm-conserving Vanderbilt (ONCV) pseudopotentials from PseudoDojo [32,33]. The accuracy of the PBE

exchange-correlation functional is tested by comparing the resulting electronic bandstructure (see Fig. S1) with the bandstructure obtained using the screened Heyd, Scuseria, and Ernzerhof (HSE) hybrid functional [34,35]. Given the close agreement for the description of the valence bands, we proceed with PBE for the rest of this work. DFPT calculation in Quantum ESPRESSO is not suitable with HSE. Therefore, carrier mobilities are determined with PBE exchange-correlation functional using the *ab initio* Boltzmann Transport Equation (aiBTE) based on phonon and ionized impurity-assisted scattering, as implemented in the EPW code [36,37]. The details about the calculation methods and convergence analysis are provided in the supplementary material (SM).

The carrier drift mobility from the linearized Boltzmann transport equation follows as:

$$\mu_{\alpha\beta} = \frac{e}{\Omega n_e}\sum_n \int \frac{d^3\mathbf{k}}{\Omega_{BZ}} v_{n\mathbf{k},\alpha}\partial_{E_\beta} f_{n\mathbf{k}}, \quad (1)$$

where, n_e is the carrier density, $v_{n\mathbf{k},\alpha}$ is the crystal group velocity of the carrier, and $\partial_{E_\beta} f_{n\mathbf{k}}$ is the perturbation from the Fermi-Dirac (FD) distribution due to external electric field **E**. Perturbation of FD function can be obtained from the self-consistent solution of the following equation:

$$\partial_{E_\beta} f_{n\mathbf{k}} = e\frac{\partial f^0_{n\mathbf{k}}}{\partial \varepsilon_{n\mathbf{k}}} v_{n\mathbf{k},\beta}\tau_{n\mathbf{k}} + \frac{2\pi\tau_{n\mathbf{k}}}{\hbar}\sum_{mv}\int \frac{d\mathbf{q}}{\Omega_{BZ}} |g_{mnv}(\mathbf{k},\mathbf{q})|^2 \times [(n_{\mathbf{q}v}+1-f^0_{n\mathbf{k}})\delta(\Delta\varepsilon^{nm}_{\mathbf{k},\mathbf{q}} + \hbar\omega_{\mathbf{q}v}) + (n_{\mathbf{q}v}+f^0_{n\mathbf{k}})\delta(\Delta\varepsilon^{nm}_{\mathbf{k},\mathbf{q}} - \hbar\omega_{\mathbf{q}v})]\partial_{E_\beta} f_{m\mathbf{k}+\mathbf{q}}. \quad (2)$$

Here, $\Delta\varepsilon^{nm}_{\mathbf{k},\mathbf{q}} = \varepsilon_{n\mathbf{k}} - \varepsilon_{m\mathbf{k}+\mathbf{q}}$, $f^0_{n\mathbf{k}}$ is the equilibrium FD distribution function, $n_{\mathbf{q}v}$ is the Bose-Einstein (BE) distribution function, and $g_{mnv}(\mathbf{k},\mathbf{q})$ is the electron-phonon (el-ph) matrix elements for scattering from initial $n\mathbf{k}$ to final $m\mathbf{k}+\mathbf{q}$ state due to a phonon mode v with crystal momentum $\mathbf{q}$ and frequency $\omega_{\mathbf{q}v}$. The quantity $\tau^{-1}_{n\mathbf{k}}$ is the electron-phonon scattering rate, which can be described as:

$$\tau^{-1}_{n\mathbf{k}} = \frac{2\pi}{\hbar}\sum_{mv}\int \frac{d\mathbf{q}}{\Omega_{BZ}} |g_{mnv}(\mathbf{k},\mathbf{q})|^2 \times [(n_{\mathbf{q}v}+1-f^0_{m\mathbf{k}+\mathbf{q}})\delta(\Delta\varepsilon^{nm}_{\mathbf{k},\mathbf{q}} - \hbar\omega_{\mathbf{q}v}) + (n_{\mathbf{q}v}+f^0_{m\mathbf{k}+\mathbf{q}})\delta(\Delta\varepsilon^{nm}_{\mathbf{k},\mathbf{q}} + \hbar\omega_{\mathbf{q}v})]. \quad (3)$$

The two Dirac delta functions represent energy-momentum conservation conditions during the el-ph scattering process, where the first term represents phonon emission and the latter term phonon absorption process. The el-ph matrix is estimated at T= 0 K, so the temperature effect on scattering as well as mobility comes from the FD and BE distribution functions. A typical method to calculate mobility using aiBTE is to neglect the second term on the right side of Eq. (2) and proceed in a non-self-consistent way, known as self-energy relaxation time approximation (SERTA) [38,39]. In this work, all phonon-limited mobility calculations are performed self-consistently using an iterative scheme to calculate $\partial_{E_\beta} f_{n\mathbf{k}}$.

Ionized impurity scatterings are calculated from first principles, using the recently implemented module in the EPW code [40,41]. With the incorporation of charge defect scattering, the total scattering rate is represented as the sum of carrier-phonon and carrier-charge defect partial scattering rates:

$$\frac{1}{\tau_{n\mathbf{k}\to m\mathbf{k}+\mathbf{q}}} = \frac{1}{\tau^{ph}_{n\mathbf{k}\to m\mathbf{k}+\mathbf{q}}} + \frac{1}{\tau^{imp}_{n\mathbf{k}\to m\mathbf{k}+\mathbf{q}}}. \quad (4)$$

Under certain approximations [41], the impurity scattering rate follows:

$$\frac{1}{\tau^{imp}_{n\mathbf{k}\to m\mathbf{k+q}}} = N_{imp}\frac{2\pi}{\hbar}\left[\frac{e^2}{4\pi\varepsilon_0}\frac{4\pi Z}{\Omega}\right]^2 \sum_{\mathbf{G}\neq\mathbf{q}} \frac{|<\Psi_{m\mathbf{k+q}}|e^{i(\mathbf{q+G}).r}|\Psi_{n\mathbf{k}}>|^2}{|(\mathbf{q+G}).\varepsilon^0.(\mathbf{q+G})|^2}\delta\left(\varepsilon_{n\mathbf{k}} - \varepsilon_{m\mathbf{k+q}}\right), (5)$$

where N_{imp} is the number of impurity carriers per unit cell of the crystal, Ze is the charge of ionized impurity, and ε^0 is the static dielectric constant [41]. To simulate the ionized impurity scattering effect in Mg-doped *p*-type ScN, fully ionized substitutional Mg impurity of charge state +2 is considered with the screening of defect potential by free carriers using the Thomas-Fermi screening model. The detail of the ionized impurity scattering scheme is provided in the SM. The Hall factor is calculated [39,42] for scaling mobility values to the experimental report of Hall mobilities accordingly.

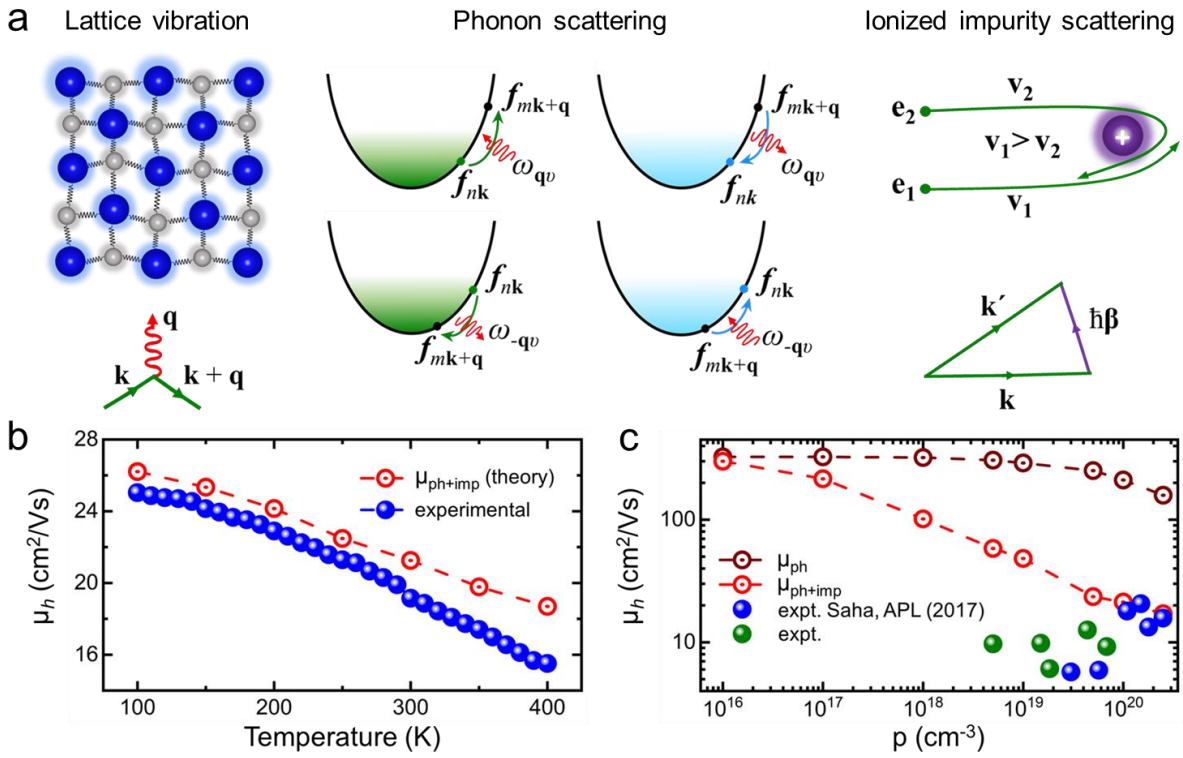

Figure 1. (a) Schematic of different carrier scattering mechanisms, such as carrier-phonon and ionized impurity scattering that governs mobility in semiconductors. Scattering of carrier out of the state ***nk*** (green) and into the state ***nk*** (sky blue) via absorption or emission of phonon mode *v* with crystal momentum ***q*** and frequency ω_{qv}. Velocity-dependent scattering of carriers from the coulomb field of ionized impurity is presented. (b) Temperature-dependent experimental Hall hole mobility of *p*-type ScN with 10^{20} cm^{-3} hole concentrations and calculated mobility from ab *initio* Boltzmann transport scheme including phonon and fully ionized impurity scattering. (c) Experimental and calculated Hall hole mobility of *p*-type ScN at room temperature as a function of the hole concentration.

For *n*-type ScN, major scattering results from the small-**q** intravalley scattering within the conduction band at the *X*-point of the Brillouin zone due to the LO phonon [43]. However, for VB, strong intra-band, as well as inter-band scattering from the LO phonon mode between different hole bands, reduce mobility. Figure 1a shows two major scattering schemes (carrier-phonon and ionized impurity scattering) that leads to low hole mobility in *p*-type ScN. Ionized

impurity creates a long-ranged coulomb potential, which scatters the carriers depending on their velocities. Under the total scattering scheme, the calculated Hall hole mobility for 10^{20} cm^{-3} hole concentration at 300K is 21 cm^2/Vs, which is close to the experimental Hall hole mobility of 18 cm^2/Vs [29] as shown in Figure 1b.

The theoretical temperature dependence of the mobility matches well with the experiment up to room temperature, beyond which, a little deviation appears due to other scattering schemes, like dislocations and other types of point defects. Further evaluation of the phonon and impurity scattering limited mobility for different hole concentrations in Figure 1c shows that for low hole density like 10^{16} cm^{-3}, carrier-phonon is the main scattering channel. The mismatch between theoretical and experimental hole mobility for lower hole concentrations is due to the consideration of screening of ionized impurity potential (see Fig. S10) and the presence of other types of defects in the sputter-deposited films. The screening in the ionized impurity scattering is essential for the non-integrable singularity of $|\mathbf{q}|^{-4}$ in impurity scattering rate [41] and for screening of ionized impurity coulomb potential with carrier concentrations of 10^{20} cm^{-3} and above. The details of impurity scattering mobility and carrier-phonon-limited hole mobility with different hole concentrations are shown in Fig. S11.

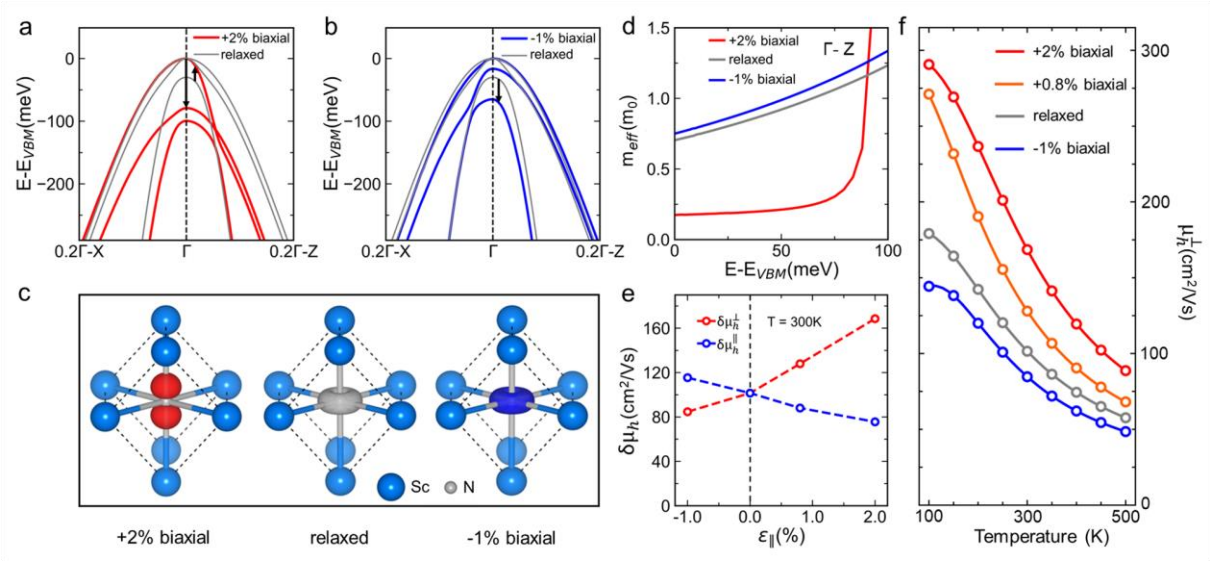

Figure 2. Strain-engineered band structure and hole mobility including el-ph and fully ionized impurity scattering in *p*-type ScN. (a), (b) PBE valence band structure of ScN under in-plane biaxial tensile and compressive strain, respectively. The energy levels have been aligned to VBM. (c) Electronic wavefunctions at the Γ-point of VBM for 2% biaxial tensile strain, relaxed, and 1% biaxial compressive strain ScN, respectively. (d) The effective mass of the topmost valence band versus the energy from VBM inside the VB. (e) Corresponding Hall hole mobility at 300 K and 10^{18} cm^{-3} carrier concentration. (f) Calculated temperature-dependent out-of-plane Hall hole mobility of ScN for relaxed and different biaxial strain cases including both el-ph and fully ionized impurity scattering effects.

One of the reasons for the low hole mobility in *p*-type ScN is also the higher effective mass of the heavy hole (hh) band. A practical way to increase mobility is to bring the light split-off hole (sh) band on top of the valence band. Figure 2a shows the strain-induced reversal of the hh and sh bands along the Γ-Z direction (out-of-plane) that reduces the effective mass of VB. The energy separation between the inverted bands along this direction is 80 meV for 2% biaxial tensile strain.

Strain-induced symmetry breaking separates hh and lh eigen energies at the zone centre (see Figure 2a and 2b). The strain affects both band ordering and the wave function characters at the VBM. Specifically, hole wavefunction at the VBM changes from the N-$p_{x,y}$ states in unstrained ScN, as shown in Figure 2c, to the N-p_z states for the biaxial-tensile strain. For biaxial-compressive strain, the character of the wave function at Γ remains the same. The calculated PBE effective mass of the sh band along the Γ-Z direction in relaxed ScN is m^*_{sh} = 0.34m_0 at the zone centre, which is lower than the effective mass of the hh band m^*_{hh} = 0.70m_0 in the same direction. For relaxed ScN, the wavefunction character of the VBM is dominated by N-p_x, and N-p_y, and the sh band is mainly from the N-p_z state near the zone centre (see Fig. S20). Therefore, this suggests, with biaxial tensile strain, band reversal occurs between the hh and sh bands along Γ-Z direction, which would improve the hole mobility of ScN. Figure 2d shows that near the zone centre along the Γ-Z direction, the effective mass of the top valence band decreases under 2% biaxial tensile strain and increases slightly for 1% biaxial compressive strain. Due to this, out-of-plane hole mobility increases for the biaxial tensile case and decreases for the biaxial compressive one. Details on the effective mass of different hole bands at the zone centre along the principal axis directions are reported in the SM (see Table S3-S6).

Transport calculations for the biaxially strained ScN including both carrier scattering mechanisms are performed. The room-temperature out-of-plane hole mobility increases by 66% from 101 cm^2/Vs unstrained value to 168 cm^2/Vs, under 2% biaxial tensile strain. On the contrary, out-of-plane hole mobility decreases by 16% for 1% biaxial compressive strain, as shown in Figure 2e. Temperature-dependent out-of-plane hole mobility of ScN for the biaxial tensile strain of 2% and of 0.8% and biaxial compressive strain of 1% (see Figure 2f) show an increase in the out-of-plane hole mobility under biaxial tensile strain.

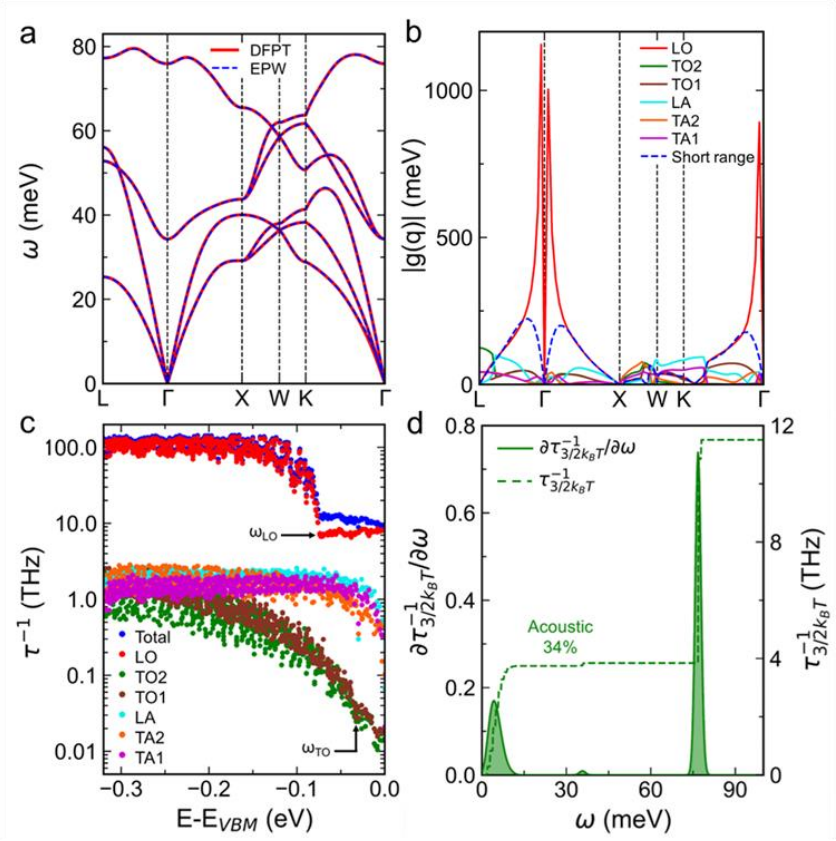

Figure 3. Phonon-mediated hole scattering rates in ScN. (a) Phonon dispersion of ScN, the solid red line is calculated from DFPT, while the broken blue line is obtained from Wannier interpolation using EPW. (b) Electron-phonon matrix elements $|g_{mnv}(\mathbf{k},\mathbf{q})|$, average on states m=3,4,5,6, and n=5,6 at $\mathbf{k}$=Γ for different phonon modes v. (c) Mode-resolved and total hole scattering rate with characteristic threshold frequency of ω_{LO} and ω_{TO} for LO and TO modes, respectively. (d) Spectral decomposed scattering rates of holes as a function of phonon energy calculated 39meV away from the VB edge. The dashed line corresponds to the cumulative integral of the spectrum, $\partial\tau^{-1}/\partial\omega$ and adds up to the carrier scattering rates τ^{-1}.

Figure 3a is the phonon band structure of relaxed ScN, with ω_{LO}= 76.0 meV and ω_{TO}= 34.3 meV in close agreement with prior work obtaining ω_{LO}= 75.8 meV and ω_{TO}= 33.4 meV at Γ [43]. Scattering from the long-range electric field due to LO phonon mode (known as Fröhlich interaction) is present in both *n*-and *p*-type ScN due to its polar semiconducting nature. Due to Fröhlich interactions, the el-ph matrix elements for the LO mode diverge as 1/ $\mathbf{q}$ for small $\mathbf{q}$ [44]. The short-range contribution of the el-ph coupling matrix suggests a weak el-ph scattering with non-polar nature, represented by the dashed blue line in Figure 3b. Along with the small-$\mathbf{q}$ intra-band scattering near Γ-point, a strong inter-band scattering between different hole bands is also present in the VB of ScN as shown in Fig. S8c.

The calculated el-ph matrix elements are used to obtain room temperature scattering rates. Figure 3c shows that total scattering is dominated by LO phonon mode with a threshold of ω_{LO}= 76.0 meV, as expected from the el-ph matrix elements. For states with an energy lower than ω_{LO}, the LO phonon absorption is the dominant scattering mechanism while above both absorption and emission of LO phonon are possible with a sharp increase of scattering rate above the threshold [43]. The contribution of TO phonon modes is much weaker in the hole scattering with a threshold of ω_{TO} below which scattering from TO mode is lower. This type of threshold energy in scattering rate is usually seen in inelastic optical phonons scattering cases. In contrast, scattering from acoustic phonons is nearly elastic without observing any characteristic threshold energy [45]. Acoustic modes' contribution in scattering is significantly stronger than the non-polar TO modes at much lower energy but noticeably the same with higher carrier energies.

This has been further validated with the spectral decomposed angular-averaged scattering rate by phonon energy at the most significant carrier energy of $3k_bT/2$ (39 meV) away from the VBM at T=300 K in Figure 3d. For unstrained and strained ScN, the main scattering channel comes from polar LO phonon mode near the Γ-point. In unstrained ScN, 34% contribution of scattering comes from long-wavelength acoustic phonon modes (peak at phonon energy of 7 meV in Figure 3d). TO phonon contributions are significantly lower for all cases except for the 2% tensile-strained case, with slightly higher contribution than others but still lower than acoustic and LO phonon contributions (see Fig. S17a). The details of spectrally decomposed scattering rates for strain cases are provided in the SM.

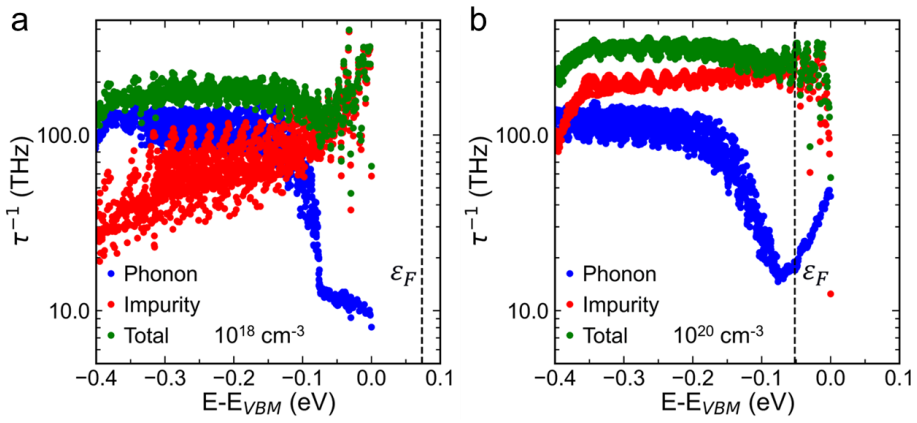

Figure 4. Phonon and ionized impurity scattering rates of holes in *p*-type ScN. Carrier scattering rates from phonon, charged impurities, and total scattering rate are obtained from first-principles for (a) 10^{18} cm^{-3}, and (b) 10^{20} cm^{-3} carrier concentrations at room temperature. The dashed line represents the Fermi level. The blue, red and green data points symbolize only phonon, ionized impurity, and total scattering rates, respectively.

Figure 4a compares different scattering effects at room temperature for 10^{18} cm^{-3} hole carrier concentration. Phonon-assisted scattering rates for 10^{20} cm^{-3} hole carrier shows a dip near the Fermi-level as in Figure 4b, which results mainly from the LO phonon scattering. The origin of the dip is due to the combination of terms inside the square brackets of Eq. (3), which reaches a minimum at ε_F [46]. With a high hole doping concentration of 10^{20} cm^{-3}, ionized impurity scattering becomes the dominant mechanism over phonon-limited scattering, reducing hole mobility in Mg-doped *p*-type ScN. The details of individual scattering limited mobility along with the Matthiessen rule for 10^{18} cm^{-3} carriers and scattering rates of other concentrations are shown in Fig S12 and Fig. S13, respectively.

Experimentally realizing tensile strain in ScN thin film can be possible via the deposition of ultra-thin ScN on top of insulating rocksalt ternary nitrides such as $MgZrN_2$, $CaTiN_2$, and $CaHfN_2$. A 1.6 % tensile strain is calculated from the lattice mismatch between $CaTiN_2$ (lattice constant of 4.58Å) and ScN [47]. Calculation of critical thickness from the Fischer model [48] shows that 2% tensile strain can be sustained in ScN thin film up to 6.8 nm thickness (see Fig. S25). Beyond that, strain relaxation occurs via the formation of misfit dislocations, which will reduce mobility further.

In summary, utilizing first-principles and the *ab initio* Boltzmann transport equation, we have shown the dominant nature of ionized impurity scattering in reducing hole mobility in Mg-doped *p*-type ScN. Large heavy hole effective mass and strong intra- and inter-band scattering due to the Fröhlich interaction also contribute to the low hole mobility. We find an effective strain-induced valence band reversal between the split-off hole and heavy hole bands with reduced valence band effective mass to increase hole mobility. We expect this work further motivates experimental research to obtain high hole mobility ScN that will lead to superior electronic and optoelectronic device applications with higher efficiencies.

Acknowledgements: SR, DR and BS acknowledge International Centre for Materials Science (ICMS) and Sheikh Saqr Laboratory (SSL) in JNCASR for support. S.P. acknowledges support

from the Fonds de la Recherche Scientifique de Belgique (F.R.S.-FNRS). B.S. acknowledges the Science and Engineering Research Board (SERB) of the Government of India, Start-Up Research Grant No. SRG/2019/000613 for financial support. SR thanks to Council of Scientific & Industrial Research (CSIR) for the fellowship. DR thanks JNCASR for the fellowship. SR and BS gratefully acknowledge the support and resources provided by PARAM Yukti Facility under the National Supercomputing Mission (NSM), Government of India at the Jawaharlal Nehru Centre for Advanced Scientific Research (JNCASR) Bangalore. DR acknowledges SAMat research facilities.

Author contributions: SR and BS conceived this project. SR performed all the EPW calculations with assistance from SP and BS. DR deposited the thin films and performed electrical measurements. SR, SP and BS analysed the results. All authors discussed and contributed to the preparation of the manuscript.

Notes: The authors declare no competing financial interest. Data is available on request from the authors.

References:

[1] S. Nakamura, *Nobel Lecture: Background Story of the Invention of Efficient Blue InGaN Light Emitting Diodes*, Rev. Mod. Phys. **87**, 1139 (2015).

[2] Z. Li, J. Waldron, T. Detchprohm, C. Wetzel, R. F. Karlicek, and T. P. Chow, *Monolithic Integration of Light-Emitting Diodes and Power Metal-Oxide-Semiconductor Channel High-Electron-Mobility Transistors for Light-Emitting Power Integrated Circuits in GaN on Sapphire Substrate*, Appl. Phys. Lett. **102**, 192107 (2013).

[3] C. Liu, Y. Cai, Z. Liu, J. Ma, and K. M. Lau, *Metal-Interconnection-Free Integration of InGaN/GaN Light Emitting Diodes with AlGaN/GaN High Electron Mobility Transistors*, Appl. Phys. Lett. **106**, 181110 (2015).

[4] C.-Y. Chang, K.-J. Wu, Y.-L. Shen, T.-L. Wu, W.-H. Kuo, S.-F. Lin, and C.-F. Huang, *Fabrication of Light-Emitting AlGaN/GaN High Electron Mobility Transistors with a Single Quantum Well Inserted*, in *2021 Device Research Conference (DRC)*, Vols. 2021-June (IEEE, 2021), pp. 1–2.

[5] T. Mimura, *The Early History of the High Electron Mobility Transistor (HEMT)*, IEEE Trans. Microw. Theory Tech. **50**, 780 (2002).

[6] H. Amano et al., *The 2018 GaN Power Electronics Roadmap*, J. Phys. D. Appl. Phys. **51**, 163001 (2018).

[7] S. Poncé, D. Jena, and F. Giustino, *Route to High Hole Mobility in GaN via Reversal of Crystal-Field Splitting*, Phys. Rev. Lett. **123**, 096602 (2019).

[8] E. C. H. Kyle, S. W. Kaun, P. G. Burke, F. Wu, Y.-R. Wu, and J. S. Speck, *High-Electron-Mobility GaN Grown on Free-Standing GaN Templates by Ammonia-Based Molecular Beam Epitaxy*, J. Appl. Phys. **115**, 193702 (2014).

[9] B. K. Ridley, B. E. Foutz, and L. F. Eastman, *Mobility of Electrons in Bulk GaN and $Al_xGa_{1-x}N$/GaN Heterostructures*, Phys. Rev. B **61**, 16862 (2000).

[10] M. Horita, S. Takashima, R. Tanaka, H. Matsuyama, K. Ueno, M. Edo, T. Takahashi, M. Shimizu, and J. Suda, *Hall-Effect Measurements of Metalorganic Vapor-Phase Epitaxy-Grown p-Type Homoepitaxial GaN Layers with Various Mg Concentrations*, Jpn. J. Appl. Phys. **56**, 031001 (2017).

[11] H. Amano, M. Kito, K. Hiramatsu, and I. Akasaki, *P-Type Conduction in Mg-Doped GaN Treated with Low-Energy Electron Beam Irradiation (LEEBI)*, Jpn. J. Appl. Phys. **28**, L2112 (1989).

[12] A. Klump, M. P. Hoffmann, F. Kaess, J. Tweedie, P. Reddy, R. Kirste, Z. Sitar, and R. Collazo, *Control of Passivation and Compensation in Mg-Doped GaN by Defect Quasi Fermi Level Control*, J. Appl. Phys. **127**, 045702 (2020).

[13] B. Saha, G. Naik, V. P. Drachev, A. Boltasseva, E. E. Marinero, and T. D. Sands, *Electronic and Optical Properties of ScN and (Sc,Mn)N Thin Films Deposited by Reactive DC-Magnetron Sputtering*, J. Appl. Phys. **114**, (2013).

[14] N. Sanders and E. Kioupakis, *Phonon- And Defect-Limited Electron and Hole Mobility of Diamond and Cubic Boron Nitride: A Critical Comparison*, Appl. Phys. Lett. **119**, 62101 (2021).

[15] S. Poncé, E. R. Margine, and F. Giustino, *Towards Predictive Many-Body Calculations of Phonon-Limited Carrier Mobilities in Semiconductors*, Phys. Rev. B **97**, 121201 (2018).

[16] B. Saha, J. Acharya, T. D. Sands, and U. V. Waghmare, *Electronic Structure, Phonons, and Thermal Properties of ScN, ZrN, and HfN: A First-Principles Study*, J. Appl. Phys. **107**, 033715 (2010).

[17] D. Rao et al., *High Mobility and High Thermoelectric Power Factor in Epitaxial ScN Thin Films Deposited with Plasma-Assisted Molecular Beam Epitaxy,* Appl. Phys. Lett. **116**, 152103 (2020).

[18] S. Acharya, A. Chatterjee, V. Bhatia, A. I. K. Pillai, M. Garbrecht, and B. Saha, *Twinned Growth of ScN Thin Films on Lattice-Matched GaN Substrates*, Mater. Res. Bull. **143**, 111443 (2021).

[19] B. Saha et al., *Cross-Plane Thermal Conductivity of (Ti,W)N/(Al,Sc)N Metal/Semiconductor Superlattices*, Phys. Rev. B **93**, 045311 (2016).

[20] B. Biswas and B. Saha, *Development of Semiconducting ScN*, Phys. Rev. Mater. **3**, 020301 (2019).

[21] P. V. Burmistrova, J. Maassen, T. Favaloro, B. Saha, S. Salamat, Y. Rui Koh, M. S. Lundstrom, A. Shakouri, and T. D. Sands, *Thermoelectric Properties of Epitaxial ScN Films Deposited by Reactive Magnetron Sputtering onto MgO(001) Substrates*, J. Appl. Phys. **113**, 153704 (2013).

[22] R. Deng, B. D. Ozsdolay, P. Y. Zheng, S. V Khare, and D. Gall, *Optical and Transport Measurement and First-Principles Determination of the ScN Band Gap*, Phys. Rev. B **91**, 045104 (2015).

[23] K. C. Maurya, D. Rao, S. Acharya, P. Rao, A. I. K. Pillai, S. K. Selvaraja, M. Garbrecht, and B. Saha, *Polar Semiconducting Scandium Nitride as an Infrared Plasmon and Phonon-Polaritonic Material.*, Nano Lett. **22**, 5182 (2022).

[24] D. Rao, A. I. K. Pillai, M. Garbrecht, and B. Saha, *Scandium Nitride as a Gateway III-Nitride Semiconductor for Both Excitatory and Inhibitory Optoelectronic Artificial Synaptic Devices*, Adv. Electron. Mater. **9**, 2200975 (2023).

[25] S. Karki, V. Rogers, P. Jadaun, D. S. Marshall, and J. A. C. Incorvia, *Large Magnetoresistance in Scandium Nitride Magnetic Tunnel Junctions Using First Principles*, Adv. Theory Simulations **4**, 2100309 (2021).

[26] D. Rao, S. Acharya, and B. Saha, *Demonstration of Compensated N-Type Scandium Nitride Schottky Diodes*, J. Phys. D. Appl. Phys. **56**, 074004 (2023).

[27] T. Ohgaki, K. Watanabe, Y. Adachi, I. Sakaguchi, S. Hishita, N. Ohashi, and H. Haneda, *Electrical Properties of Scandium Nitride Epitaxial Films Grown on (100) Magnesium Oxide Substrates by Molecular Beam Epitaxy*, J. Appl. Phys. **114**, 93704 (2013).

[28] Y. Oshima, E. G. Villora, and K. Shimamura, *Hydride Vapor Phase Epitaxy and Characterization of High-Quality ScN Epilayers*, J. Appl. Phys. **115**, (2014).

[29] B. Saha, M. Garbrecht, J. A. Perez-Taborda, M. H. Fawey, Y. R. Koh, A. Shakouri, M. Martin-Gonzalez, L. Hultman, and T. D. Sands, *Compensation of Native Donor Doping in ScN: Carrier Concentration Control and p-Type ScN*, Appl. Phys. Lett. **110**, 252104 (2017).

[30] P. Giannozzi et al., *Advanced Capabilities for Materials Modelling with Quantum ESPRESSO*, J. Phys. Condens. Matter **29**, 465901 (2017).

[31] J. P. Perdew, K. Burke, and M. Ernzerhof, *Generalized Gradient Approximation Made Simple*, Phys. Rev. Lett. **77**, 3865 (1996).

[32] D. R. Hamann, *Optimized Norm-Conserving Vanderbilt Pseudopotentials*, Phys. Rev. B - Condens. Matter Mater. Phys. **88**, 085117 (2013).

[33] M. J. van Setten, M. Giantomassi, E. Bousquet, M. J. Verstraete, D. R. Hamann, X. Gonze, and G.-M. Rignanese, *The PseudoDojo: Training and Grading a 85 Element Optimized Norm-Conserving Pseudopotential Table*, Comput. Phys. Commun. **226**, 39 (2018).

[34] J. Heyd, G. E. Scuseria, and M. Ernzerhof, *Hybrid Functionals Based on a Screened Coulomb Potential*, J. Chem. Phys. **118**, 8207 (2003).

[35] J. Heyd, G. E. Scuseria, and M. Ernzerhof, *Erratum: Hybrid Functionals Based on a Screened Coulomb Potential (Journal of Chemical Physics (2003) 118 (8207))*, J. Chem. Phys. **124**, 219906 (2006).

[36] S. Poncé, E. R. Margine, C. Verdi, and F. Giustino, *EPW: Electron–Phonon Coupling, Transport and Superconducting Properties Using Maximally Localized Wannier Functions*, Comput. Phys. Commun. **209**, 116 (2016).

[37] F. Giustino, M. L. Cohen, and S. G. Louie, *Electron-Phonon Interaction Using Wannier Functions*, Phys. Rev. B - Condens. Matter Mater. Phys. **76**, 165108 (2007).

[38] F. Giustino, *Electron-Phonon Interactions from First Principles*, Rev. Mod. Phys. **89**, 015003 (2017).

[39] S. Poncé, F. Macheda, E. R. Margine, N. Marzari, N. Bonini, and F. Giustino, *First-Principles Predictions of Hall and Drift Mobilities in Semiconductors*, Phys. Rev. Res.

3, 043022 (2021).

[40] H. Lee et al., *Electron-Phonon Physics from First Principles Using the EPW Code*, arXiv:2302.08085v1.

[41] J. Leveillee, X. Zhang, E. Kioupakis, and F. Giustino, *Ab Initio Calculation of Carrier Mobility in Semiconductors Including Ionized-Impurity Scattering*, Phys. Rev. B **107**, 125207 (2023).

[42] F. Macheda and N. Bonini, *Magnetotransport Phenomena in p -Doped Diamond from First Principles*, Phys. Rev. B **98**, 201201 (2018).

[43] S. Mu, A. J. E. Rowberg, J. Leveillee, F. Giustino, and C. G. Van De Walle, *First-Principles Study of Electron Transport in ScN*, Phys. Rev. B **104**, 075118 (2021).

[44] C. Verdi and F. Giustino, *Fröhlich Electron-Phonon Vertex from First Principles*, Phys. Rev. Lett. **115**, 176401 (2015).

[45] M. Lundstrom, *Fundamentals of Carrier Transport*, (Cambridge University Press, Cambridge, 2009).

[46] K. Krishnaswamy, B. Himmetoglu, Y. Kang, A. Janotti, and C. G. Van De Walle, *First-Principles Analysis of Electron Transport in BaSnO3*, Phys. Rev. B **95**, 205202 (2017).

[47] S. R. Bauers et al., *Ternary Nitride Semiconductors in the Rocksalt Crystal Structure*, Proc. Natl. Acad. Sci. U. S. A. **116**, 14829 (2019).

[48] A. Fischer, H. Kiihne, and H. Richter, *New Approach in Equilibrium Theory for Strained Layer Relaxation*, **73**, (1994).